

Learn to Demodulate: MIMO-OFDM Symbol Detection through Downlink Pilots

Zhou Zhou, Lingjia Liu, and Hao-Hsuan Chang

Bradley Department of Electrical and Computer Engineering, Virginia Tech.,
Blacksburg, VA, USA, 26041

Abstract

Reservoir computing (RC) is a special neural network which consists of a fixed high dimensional feature mapping and trained readout weights. In this paper, we consider a new RC structure for MIMO-OFDM symbol detection, namely windowed echo state network (WESN). It is introduced by adding buffers in input layers which brings an enhanced short-term memory (STM) of the underlying neural network through our theoretical proof. A unified training framework is developed for the WESN MIMO-OFDM symbol detector using both comb and scattered pilot patterns, where the utilized pilots are compatible with the structure adopted in 3GPP LTE/LTE-Advanced systems. Complexity analysis reveals the advantages of the WESN based symbol detector over the state-of-the-art symbol detectors such as the linear the minimum mean square error (LMMSE) detection and the sphere decoder when the system is employed with a large number of OFDM sub-carriers. Numerical evaluations corroborate that the improvement of the STM introduced by the WESN can significantly improve the symbol detection performance as well as effectively mitigate model mismatch effects as opposed to existing methods.

Index Terms

Machine learning, OFDM, MIMO, symbol detection, reservoir computing, echo state network, LTE-Advanced, and pilot patterns

I. INTRODUCTION

Multiple-input, multiple-output, orthogonal frequency-division multiplexing (MIMO-OFDM) is the dominant wireless access technology for 4G and 5G cellular networks. The powerful combination of MIMO and OFDM, MIMO-OFDM, enables the wireless system to achieve

high spectral-efficiency over broadband channels with simplified transceiver architectures. MIMO technology introduces additional spatial degrees of freedom and enables various multi-antenna transmission strategies such as transmit diversity, spatial multiplexing, and multi-user MIMO operations [1] to improve overall network performance. To achieve the spatial-multiplexing gain in MIMO systems, different data streams are transmitted from different antennas causing inter-streams interference at the receiver. Accordingly, the symbol detection of multiple transmitted symbols from receiving antennas becomes critical for MIMO to realize its promise. This means that the performance of MIMO systems depends heavily on the underlying detection algorithm at the receiver. In general, MIMO detection is classified into coherent detection and noncoherent detection [2]. In the coherent MIMO detection, the instantaneous channel matrix is obtained at the receiver through explicit channel estimation. In this way, a two-step approach is adopted where the instantaneous channel matrix is estimated in the first step while MIMO symbol detection is conducted in the second step based on the estimated channel matrix as well as the received signals. On the other hand, in noncoherent detection, the channel estimation is either performed implicitly or is completely avoided. However, channel statistics are typically assumed at the receiver to support noncoherent detection. Furthermore, noncoherent MIMO detection schemes usually apply differential encoding on input symbols leading to higher computational complexity. Therefore, most modern wireless systems use coherent MIMO detection instead of noncoherent MIMO detection.

Meanwhile, OFDM technology combats the effect of frequency-selective fading by breaking a wide-band channel into multiple orthogonal flat-fading narrow-band channels. This significantly simplifies the transceiver architecture of the underlying wireless system making it the most popular multiple-access strategy of modern wireless systems including both cellular and WiFi. However, the underlying time-domain waveform usually has a high peak-to-average power ratio (PAPR), as a result from the multi-carrier nature of the OFDM transmission. This high PAPR has negative impacts on power amplifiers (PAs) by producing signal excursions into the PA's non-linear operation region leading to non-linear distortions and spectral regrowth [3]. Furthermore, non-linear distortion has a significant negative impact on the estimation of MIMO-OFDM channels making MIMO-OFDM detection challenging. Therefore, PAPR reduction strategies are introduced together with power back-off to mitigate the non-linear distortion by enabling the input waveform to operate in PA's linear region. In order to address the nonlinear distortion

as well as the clipping noise, more resources on transmission and computations are required to recover the distortion, such as the decision aided method in [4] and the iterative estimation in [5]. Alternatively, the digital pre-distortion (DPD), can be introduced ahead of the PA to compensate for PA's non-linearity effects allowing operations closer to the maximum rated power while maintaining low spectral regrowth [6]. Then, neural networks can be utilized for the DPD design [7], [8] which can reduce the performance loss in channel estimation and signal detection. However, it is important to note that a perfect knowledge of PA modeling and measurement bias is required in order for the DPD to compensate for the non-linear effect. Without this knowledge, the underlying effective channel becomes non-linear which poses a challenge for MIMO-OFDM detection. Meanwhile, obtaining the perfect knowledge related to PA modeling and measurement bias is very demanding in reality [9]. Therefore, it is desirable to have a MIMO-OFDM detection strategy that is robust to the underlying non-linear distortion. The fulfillment can bring additional benefits as well, such as an improved PA transmission efficiency.

On the other hand, artificial neural networks (ANNs) as an emerging technology provides new aspects to solve communications problems. For instance, in [10]–[12], auto-encoder is considered as a way to interpret the symbol modulation in communications system, in which transmitters and receivers are learned through an end to end training by minimizing the metrics of transmission reliability. However, in practical systems, this end to end learning strategy requires heavy feedbacks and computations. Therefore, employing ANNs as functional components in a communications link instead of replacing the whole link as ANNs is an alternative way in the applications. Previous works [13]–[15] use RNN as the receiver in molecular communications system, where the underlying channel is unavailable to be modeled. Moreover, in optical fiber systems [16], [17], ANNs are utilized as a channel equalizer as well as a network monitor.

In light of the challenge in MIMO-OFDM symbol detection, ANNs provide an ideal framework to conduct the symbol detection even under the non-linear distortion. In [18], it introduces using a deep neural network for OFDM symbol detection without using explicit CSI. The learning procedure is composed of an offline and an online training and shows the deep ANN performs a lower bit error rate (BER) than the minimum mean squared estimator (MMSE) under a non-linear distortion channel. However, the offline training stage is conducted according to an assumption on channel statistics. In [19], it introduced a neural network based method for the receiver design in a CP-free OFDM system. In [20], a fully connected neural network based OFDM receiver is

tested over the air. However, the extension to the MIMO-OFDM system is not investigated in these aforementioned works. To study the MIMO case, in [21], a deep neural network detector is introduced based on unfolding the standard belief propagation algorithm. The neural network parameters are further tuned via an offline training which requires enormous investigations for various antenna configurations. In [22], the feature of residual signals after layered processing is applied to construct a neural network for symbol detection. Meanwhile, the loss function is conducted on multiple layers in order to avoid the gradient vanishing [23]. It demonstrates the introduced network can perform as well as the spherical decoding while achieving lower computational complexity. However, these methods require pre-known CSI as the coefficients or the inputs of neural networks which cannot be perfectly obtained due to channel distortion.

From the aforementioned examples, feedforward neural networks are employed for symbol detection by dividing the received signal into independent batches. However, the signal in communications system is sequentially constructed. Therefore, using recurrent neural networks (RNNs) allows learning to the extent of temporal dynamical behaviors [24]. In RNNs, the current outputs are fed to inputs for the future processing. In standard RNN inference, the weights learning of the RNNs are calculated by the backpropagation through time algorithm (BPTT) [25]. However, the training of RNNs is very challenging, especially when the sequence is inherent with long-range temporal dependencies. This is because of the gradient vanishing and exploding effect during the BPTT procedure, i.e., a small change at the current iteration can result in a very large deviation for later iterations [26]. This problem of gradient vanishing and exploding make the optimization of RNNs for sequences with long-range temporal dependencies challenging. To combat this, some special structures are introduced to avoid the training problem in RNNs, like the long short-term memory network [27] which uses memory units and gating units to control the gradient flow in order to avoid the gradient vanishing.

Furthermore, rooted from the backpropagation-decorrelation learning rule, RC is one type of RNNs, in which the weights-learning of RC can naturally avoid the issues of RNN training, and meanwhile achieves high computational efficiency [28]. The learning is neither conducted on inputs nor hidden layers, but only on outputs. Meanwhile, the untrained layers are sampled from the distribution with well-designed conditions. An RC-based MIMO-OFDM symbol detector is first introduced in our previous work [29], [30]. With limited training, [29] shows that the RC-based symbol detector can effectively combat the non-linear distortion caused by PA. However,

our previous introduced RC-based symbol detector has a very simple neural network architecture and does not work well for scattered pilot patterns. In this paper, we further develop the RC-based symbol detector for MIMO-OFDM by improving the architecture of the underlying RC-based symbol detector and introducing a training framework which is compatible with different pilot patterns. In numerical evaluations, we show the advances of this short term memory enhanced structure via the BER.

The detailed contributions of our paper are summarized as follows

- We incorporated buffers¹ in the input layer of RC, i.e, WESN. Through theoretical analysis, we proved that the added buffer can improve the short term memory of the underlying RC. Numerical evaluations demonstrate the RC with improved short-term memory can perform better interference cancellation in the MIMO-OFDM system.
- We introduced a unified training method for the WESN using the pilot pattern which is compatible with the demodulation reference signal (DMRS) proposed in LTE/LTE-Advanced standards. Meanwhile, we demonstrated the RC can detect symbols using non-orthogonal pilots through numerical evaluations.
- We analyzed the complexity of the RC-based symbol detector compared to conventional MIMO-OFDM receivers, such as LMMSE and sphere decoding which is an approximation to the maximum likelihood estimator [31], [32]. The results suggest that the RC-based detector has less computational complexity than conventional methods, especially when a large number of sub-carriers are utilized.

The structure of this paper is organized as follows: In Sec. II, the system model of MIMO-OFDM and conventional symbol detection methods are introduced. Meanwhile, the preliminary knowledge of reservoir computing is reviewed. In Sec. III, the WESN based MIMO-OFDM symbol detector as well as the pilot structure are discussed. In addition, the analysis of the short term memory of WESN is presented in this section. The complexity comparison between conventional methods and the RC-based method is discussed in Sec. IV. In Sec. V, the performance of WESN is evaluated. Finally, conclusions are given in Sec.VI.

¹the buffer represents a linear shift register without any feedback tap

II. SYSTEM MODEL AND PRELIMINARIES

A. Channel Model and Transmitter Architecture

We now consider the point to point MIMO-OFDM system, where the number of Tx and Rx antennas are respectively denoted as N_t and N_r . At the p th transmitted antenna, the i th OFDM symbol is expressed as

$$u_i^{(p)}(t) = \sum_{n=0}^{N_c-1} x_i^{(p)}[n] \exp(2\pi j n t / \Delta t), t \in [i\Delta t, (i+1)\Delta t) \quad (1)$$

where $x_i^{(p)}[n]$ is the transmitted symbol at the n th sub-carrier, N_c stands for the number of sub-carriers, Δt is the time length of one OFDM symbol. At the q th antenna, the corresponding received OFDM symbol is given by

$$y_i^{(q)}(t) = \sum_{p=0}^{N_t-1} h_i^{(q,p)}(t) \otimes g(u_i^{(p)}(t)) + n(t) \quad (2)$$

where $n(t)$ represents the additive noise, \otimes stands for the circular convolution which is translated by the circular prefix of an OFDM symbol, $g(\cdot)$ is a general notation of the waveform distortion which is discussed later in this section, and $h_i^{(q,p)}(t)$ is the channel response from the p th Tx antenna to the q th Rx antenna for the i th OFDM symbol. Here, we assume that the channel is given by the following tap-delay model:

$$h_i^{(q,p)}(\tau) = \sum_{l=0}^{L-1} a_i^{(p,q)}(l) \delta(\tau - \tau_l) \quad (3)$$

where L is the maximum number of resolvable paths and $\delta(\tau)$ is the Dirac delta function. At the l th delay tap, we assume $a_i(l)$ is generated by the circular Gaussian distribution,

$$a_i(l) \sim \mathcal{NC}(0, \sigma_l^2)$$

where σ_l^2 is assumed to be an exponential power delay profile, i.e., $\sigma_l^2 = \exp(-\alpha \tau_l / \tau_{\max})$. Moreover, between two adjacent OFDM symbols, the correlation is assumed to be

$$\mathbb{E}(a_i(l)a_{(i+1)}(l)) = \sigma_l^2 J_0(2\pi f_D \Delta t) \quad (4)$$

where J_0 stands for the Bessel function of the first kind with parameter 0. Equivalently, the signal model (2) can be expressed in the digital frequency domain as

$$\tilde{y}_i^{(q)}[n] = \sum_{p=0}^{N_t-1} \tilde{h}_i^{(p,q)}[n] \tilde{g}^{(p)}[n] + \tilde{n}[n] \quad (5)$$

where $\tilde{n}[n]$ is the additive noise on the frequency domain,

$$\tilde{g}^{(p)}[n] = \int_{\Delta t} g(u_i^{(p)}(t)) e^{-2\pi jtn/\Delta t} dt \quad (6)$$

$$\tilde{h}_i^{(p,q)}[n] = \int_{\Delta t} h_i^{(p,q)}(\tau) e^{-2\pi n j\tau/\Delta t} d\tau \quad (7)$$

Specifically, when we set $g(z_i^{(p)}(t)) = z_i^{(p)}(t)$, we have

$$\tilde{y}_i^{(q)}[n] = \sum_{p=0}^{N_t-1} \tilde{h}_i^{(p,q)}[n] x_i^{(p)}[n] + \tilde{n}[n] \quad (8)$$

Now, we consider the signal waveform distortion $g(\cdot)$ at the transmitter. In the OFDM system, after the OFDM waveform is converted into the analog domain, it passes through RF circuits, such as power amplifiers, filters, and delay lines. These analog components are imperfect linear systems due to practical efficiency constraints, such as circuit spaces and power consumptions. For instance, the power amplifier (PA) is modeled by the following RAPP model [33]:

$$g(u(t)) = \frac{G_0 u(t)}{[1 + (\frac{|u(t)|}{u_{sat}})^{2p}]^{1/2p}} \quad (9)$$

where $u(t)$ is the input signal of PA, G_0 stands for the power gain of PA, u_{sat} is the saturation level, and $p > 0$ is the smooth factor. By looking at this nonlinear behavior of PA as shown in Fig. 1, we know that the operational region of PA can be generally divided into three parts: the linear region $|u(t)| \ll u_{sat}$, the non-linear region $|u(t)| \sim u_{sat}$, and the saturation region $|u(t)| \gg u_{sat}$. Meanwhile, it is also known that the power efficiency is lower in the linear region, even though the signal waveform is perfectly retained. Thus, the PA operational point is set close to the nonlinear region in order to achieve higher PA efficiency. Meanwhile, due to the high peak average power ratio (PAPR) of the OFDM signal, PAPR reduction is also employed to guarantee a certain level of PA efficiency [3]. However, all these involved selections on efficiency lead to the deficiency in transmission reliability due to waveform distortion. A similar trade-off between efficiency and reliability exists in the design of other circuit components as well. Generally, we denote the resulting imperfectness as the function $g(\cdot)$.

B. Conventional Methods

Conventional symbol detection methods are conducted by two steps. In the beginning, Tx sends a series of pre-known pilots $\tilde{x}_i^p[n]$ to Rx for the channel estimation, where $i \in \Omega_t$, $p \in \Omega_s$,

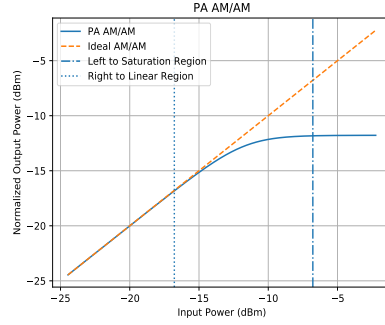


Fig. 1: The input and output amplitude (AM/AM) curve of PA : $p = 3$ and $|u_{sat}|^2 = -11.78dB$

$n \in \Omega_f$ in which Ω_t , Ω_s and Ω_f respectively represents the pilots index sets of OFDM symbols, antennas, and sub-carriers. Specifically, in the LTE standard, the design of pilot patterns is based on resource blocks (RB) divisions as shown in Fig. 2. For the SISO case, it is depicted in Fig. 2 (a). The first sub-figure illustrates that Ω_t equals to the first OFDM symbol and Ω_f occupies the whole sub-carriers. This comb pattern is applied to the block fading channel assumption, i.e., $f_D = 0$ Hz. Moreover, the size of Ω_f can be further reduced as shown in the second sub-figure of Fig. 2 (a), as the channel interpolation can be incorporated by frequency coherence. Furthermore, in the third subfigure of Fig. 2 (a), the scattered pilot pattern is applied on a Doppler channel which facilitates the channel tracking with mid pilot consumption. For the MIMO channel, the pilot pattern is shown in Fig. 2 (b) and 2 (c). In Fig. 2 (b), the pilot symbols at different antenna ports are without overlapping each other since they are allocated to different OFDM symbols. In Fig. 2 (c), the cross marker represents the null pilot symbols. Thus, the pilot interference is free during the channel estimation stage for MIMO. Therefore, the channel estimation on each Tx and Rx antenna pair becomes the SISO as the case in Fig. 2 (a).

Thereafter, the channel fading coefficients on the allocated grids can be obtained through (5) by solving

$$\min_{\tilde{h}_i^{(p,q)}[n]} l(\tilde{y}_i^{(q)}[n], \tilde{x}_i^{(p)}[n]) | (i, p, n) \in \Omega_t \times \Omega_s \times \Omega_f \quad (10)$$

where $l()$ is a pre-defined loss-function, such as likelihood function, mean square error, etc.. Then through an interpolation, the CSI on the remained grids can be inferred. Finally, by substituting the estimated $\hat{h}_i^{(p,q)}[n]$ into (5), the rest symbols $\{x_i^{(p)}[n] | (i, p, n) \in \Omega_t^c \times \Omega_s^c \times \Omega_f^c\}$, where Ω^c

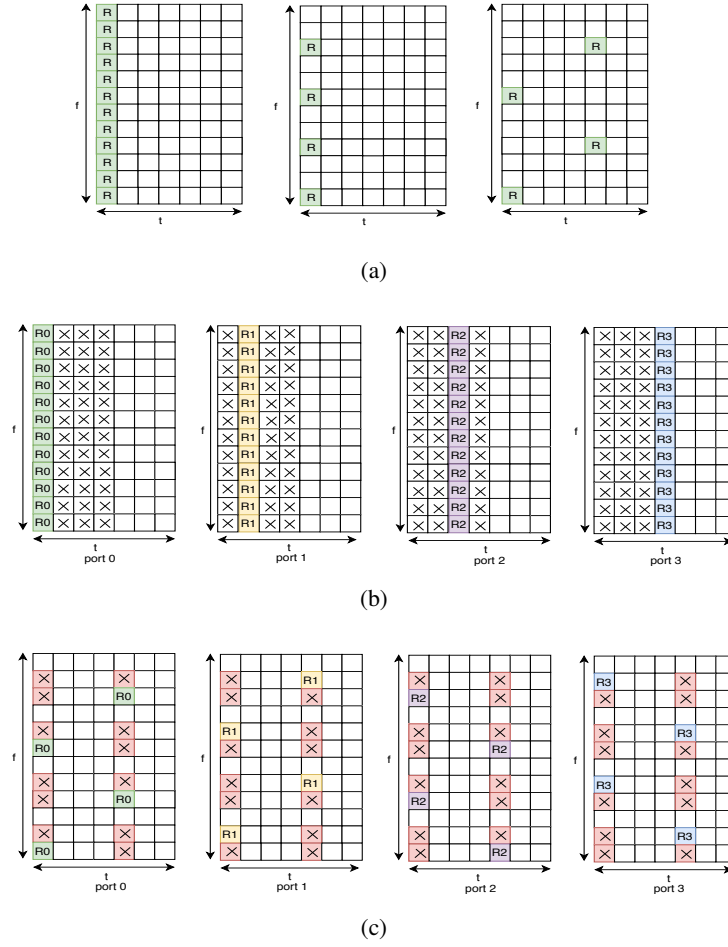


Fig. 2: OFDM Pilot Structure in one RB (a) SISO-OFDM pilots (b) Comb Structured MIMO-OFDM pilots (c) Scattered Structured MIMO-OFDM pilots

stands for the complementary set of Ω , can be generally estimated by

$$\min_{x_i^p[n]} l(\hat{y}_i^{(q)}[n], \hat{h}_i^{(p,q)}[n]) | (i, p, n) \in \Omega_t^c \times \Omega_s^c \times \Omega_f^c \quad (11)$$

Note that the above channel estimation and detection are conducted through the frequency domain. This is because of the simplicity of converting convolution into multiplying by the Fourier transform. More discussions on existing methods will be presented in Sec. IV,

However, the optimality on solving (10) and (11) cannot be generally guaranteed due to the knowledge scarcity on the nonlinear function $g(\cdot)$ or its inherent non-convexity. Most importantly, an improper assumption on $g(\cdot)$ can cause the model mismatch which deteriorates the accuracy on solving the estimation problem (10) and the detection problem (11). To circumvent this dilemma, i.e., the dependence on the model assumption, RC based method can be employed

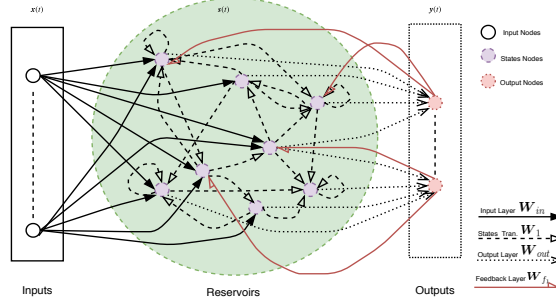


Fig. 3: An Example of Reservoir Computing: Echo-State Network Architecture

as an alternative solution.

C. Reservoir Computing

Before proceeding on how to incorporate RC into the symbol detection problem, we briefly introduce the basic structure of RC. RC is one category of RNNs which consists of an input layer mapping input signal into a higher dimension, a fixed dynamic system, and a trained readout network. Echo state network (ESN) [28] as illustrated in Fig. 3 is one realization of RC. The dynamics of ESN is described by the following equation

$$\mathbf{s}(t+1) = f_{states}(\mathbf{W}'[\mathbf{y}^T(t+1), \mathbf{s}^T(t), \mathbf{x}^T(t)]^T) \quad (12)$$

where $\mathbf{s}(t) \in \mathbb{C}^{N_n}$ represents the inner states, N_n is the number of neurons inside the reservoir, $\mathbf{y}(t)$ is the input signal, f_{states} represents the states activation function, $\mathbf{W}' = [\mathbf{W}_{in}, \mathbf{W}_1, \mathbf{W}_{f1}]$, where \mathbf{W}_{in} is weights of the input layer, \mathbf{W}_1 is the inner state transition weights, and \mathbf{W}_{f1} is weights of the feedback layer. Moreover, \mathbf{W}_{f1} can be void when feedback is not required. The output equation is given by

$$\mathbf{x}(t+1) = f_{out}(\mathbf{W}_{out}\mathbf{s}^T(t+1)) \quad (13)$$

where f_{out} is the activation function defined by training tasks, and \mathbf{W}_{out} represents the output layer. To drive the ESN to work, the states transition weights \mathbf{W}' are designed according to the following *echo state property*,

Definition 1: We consider an ESN following the state transition equation defined in (12). Given an input sequence $\mathbf{x}(t)$ and two finite initial states $\mathbf{s}_1(0)$ and $\mathbf{s}_2(0)$, for any $\epsilon > 0$ and $\mathbf{x}(t)$, if we have $\|\mathbf{s}_1(t) - \mathbf{s}_2(t)\| < \epsilon$ when $t > \delta(\epsilon)$, then the ESN satisfies the echo state property.

Nevertheless, the echo state property of a given ESN cannot be easily justified from the above definition. For ease of application, the following sufficient condition is usually applied.

Theorem 1 (Proposition 3 in [28]): Assume an ESN with $\tanh(\cdot)$ as the states activation function. If the maximum singular value of the inner states transition weight matrix \mathbf{W} is smaller than 1, i.e., $\sigma(\mathbf{W})_{max} < 1$, then for all input $\mathbf{x}(t)$ and initial states $\mathbf{s} \in [-1, 1]^N$, the ESN satisfies the echo state property.

For the learning of output weights \mathbf{W}_{out} , it contains the following two stages:

- Generation of the states trajectory: By feeding the training input $\{\bar{\mathbf{y}}(t)\}_{t=0}^T$ into ESN with target $\{\bar{\mathbf{x}}(t)\}_{t=0}^T$, the states set $\{\bar{\mathbf{s}}(t)\}_{t=0}^T$ is obtained by (12), where T represents the sequence length of the training input.
- Regression on the output weights: Substituting the generated states $\{\bar{\mathbf{s}}(t)\}_{t=0}^T$ into (13), we can calculate the weights \mathbf{W}_{out} through

$$\min_{\mathbf{W}_{out}} L(\{\bar{\mathbf{y}}(t)\}_{t=0}^T, \{f_{out}(\mathbf{W}_{out}\bar{\mathbf{s}}^T(t))\}_{t=0}^T) \quad (14)$$

Specifically, when we choose f_{out} as a linear function, L as Frobenius norm, the output weights are solved by

$$\min_{\mathbf{W}_{out}} \sum_{t=0}^T \|\bar{\mathbf{y}}(t) - \mathbf{W}_{out}\bar{\mathbf{s}}(t)\| \quad (15)$$

which has a close form solution as

$$\mathbf{W}_{out} = \bar{\mathbf{Y}}\mathbf{S}^+ \quad (16)$$

where $\bar{\mathbf{Y}} = [\bar{\mathbf{y}}(0), \dots, \bar{\mathbf{y}}(T)]$, $\mathbf{S} = [\mathbf{s}^T(0), \dots, \mathbf{s}^T(T)]$, and \mathbf{S}^+ is the MoorePenrose inverse of \mathbf{S} .

III. SYMBOL DETECTION

In this section, we will introduce our symbol detection approach. We begin by explaining the concept of neural network based symbol detection. Then, we introduce the WESN for MIMO symbol detection.

A. Neural Network Based Approach

The neural network based symbol detection consists of two steps, the training and the testing stage. In the training stage, base station (BS) sends pre-defined symbols $\{\bar{x}_i^{(p)}[n] | (i, p, n) \in$

$\Omega_t \times \Omega_s \times \Omega_f$ to mobile stations (MSs). Then, MSs train the neural network receiver \mathcal{D} by solving

$$\min_{\mathcal{D}} f(\mathcal{D}(y_i^{(p)}(t)), \bar{x}_i^{(p)}[n] | (i, p, n) \in \Omega_t \times \Omega_s \times \Omega_f) \quad (17)$$

where $f(\cdot)$ is the training objective function and \mathcal{D} is the neural network. For instance, $f(\cdot)$ can be the mean squared error or the cross-entropy; \mathcal{D} can be the fully connected, convolution or recurrent neural networks. In the testing stage, the symbols are estimated by feeding the observation $y_i^{(p)}(t)$ to the learned neural network $\hat{\mathcal{D}}$, i.e., $\hat{\mathcal{D}}(y_i^{(p)}(t))$. Consequently, the symbol detection performance and the implementation complexity are determined by the neural networks structure and the learning method. However, in communications systems, the resources allocated to pilots are less than the transmitted data symbols due to the limited bandwidth. Therefore, underfitting can occur if the adopted NN structure is improper.

B. Windowed Echo State Network

Before proceeding on the WESN based symbol detection, we first consider the short term memory of WESN.

1) *ESN Short Term Memory*: For RNN, the output features are expected to be a certain function of the memory encoded from inputs. Therefore, longer memory allows longer time-scaled features be learned. Intuitively, the memory ability can be measured by testing the recovering of historical inputs. Thus, the memory capacity of ESN is defined as follows,

Definition 2 (Short Term Memory [34]): Given an ESN with fixed coefficients of the inner state transient matrix, input layer, and activation function, we first define the following *self-delay reconstruction correlation*

$$d(m, \mathbf{w}_{out}) = \frac{\text{cov}^2(y(n-m), x(n; m))}{\sigma^2(y(n-m))\sigma^2(x(n; m))} \quad (18)$$

where \mathbf{w}_{out} is the output weights for the ESN with a single input and a single output; With a slight abuse of notations, in this subsection, n represent the time sequence index, m is the input delay degree, and $x(n; m)$ is the ESN output when input is $y(n-m)$. Then, relying on the self-delay reconstruction correlation, we have the following definitions,

- The m th delay STM capacity:

$$MC_m = \max_{\mathbf{w}_{out}} d(m, \mathbf{w}_{out}) \quad (19)$$

- The STM capacity:

$$MC = \sum_{m=1,2,\dots} MC_m \quad (20)$$

Remark that the above definition is only for ESN with a single input and a single output. The general definition of STM for ESN with multiple inputs and multiple outputs is obtained by extending the concept to each input-output pair. Furthermore, the metric in (19) can be approximately calculated through the self-delay training procedure defined as follows: 1) Input the zero mean sequence $\{y(n)\}_{n=0}^{N-1}$ to ESN; 2) Train the ESN's output using the target $\{y(n)\}_{n=0}^{N-m-1}$. Therefore, the *self-delay reconstruction correlation* can be rewritten as

$$d(m, \mathbf{w}_{out}) = \frac{|\sum_{n=0}^{N-m-1} x(n)y_i(n+m)|}{\sqrt{\sum_{n=0}^{N-m-1} |x(n)|^2} \sqrt{\sum_{n=m}^{N-1} |y_i(n)|^2}} \quad (21)$$

$$\propto -\|\tilde{\mathbf{y}}(m : N-1) - \tilde{\mathbf{x}}(0 : N-m-1)\|_2^2 \quad (22)$$

where \propto stands for in a relation of proportionality; $\tilde{\mathbf{y}}(m : N-1)$ is a normalized vector stacked by the samples from $y(m)$ to $y(N-1)$ and $\tilde{\mathbf{x}}(0 : N-m-1)$ is defined similarly. Then, the output weights in (19) can be calculated by solving

$$\mathbf{w}_{out} = \tilde{\mathbf{x}}(0 : N-m-1) \mathbf{S}^+ \quad (23)$$

where $\mathbf{S} = [\mathbf{s}^T(m), \mathbf{s}^T(m+1), \dots, \mathbf{s}^T(N-1)]$. From the above definition, we can obtain the STM capacity of a buffer as follows

Theorem 2: The memory capacity of a buffer is greater than M , where M is the buffer's size.

Proof: For a buffer, it is easily known that $MC_m = 1$ if $0 \leq m \leq M$. When $m > M$, we have $MC_m \geq 0$ as the signal can be self-correlated. Therefore, we have $MC_W \geq M$. ■

Furthermore, we have the following upper bound for the STM capacity of ESN

Theorem 3 (Proposition 2 in [34]): The memory capacity of ESN is bounded by the number of neurons, i.e., $MC_{ESN} < N_n$.

Note that the above conclusion can only be made when the network is with a linear output activation and an i.i.d input. However, this theorem can give us a general guide on setting the number of neurons. For more details, please refer to the discussions in the evaluation part of this paper. By the comparison between Theorem 2 and Theorem 3, we see the buffer has a higher STM capacity than the ESN when the buffer size is the same as the number of neurons

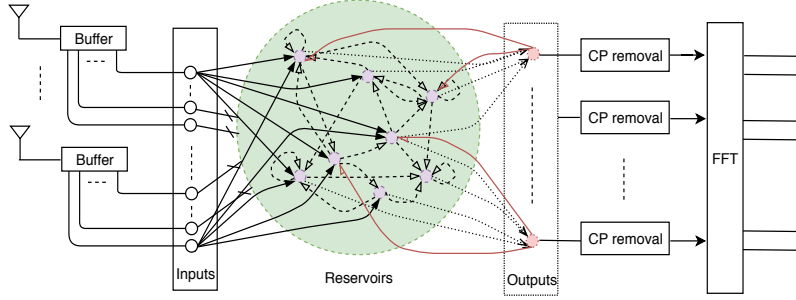


Fig. 4: The architecture of Windowed Echo-State Network MIMO-OFDM detector

of the ESN. However, a higher STM capacity does not necessary stand for a better nonlinear feature mapping ability. This is because reservoirs process the memory of inputs through a highly nonlinear recursive procedure rather than simply storing the inputs. Now, we consider the STM capacity of WESN. The WESN is constructed by adding buffers at ESN's inputs as depicted in Fig. 4. For the STM of WESN, we can obtain the following result

Theorem 4: Given a WESN, suppose the STM capacity of the buffer and the ESN component are MC_W and MC respectively. Then, the STM capacity of WESNs, MC_{WESN} , is followed by

$$MC_{WESN} \geq \lambda MC_W + (1 - \lambda)MC_{ESN}, \lambda \in (0, 1) \quad (24)$$

Proof: See Appendix VI.2 for details ■

The above result shows that WESN can achieve a higher STM capacity than the sum of the STMs of the buffer and the ESN.

C. WESN based MIMO-OFDM receiver

Our introduced WESN based MIMO-OFDM symbol detector is plotted in Fig. 4. We see the receiving link is concatenated by a WESN, a cyclic prefix (CP) removal and an FFT block, where the dimension of WESN's outputs is the same as the number of transmission streams. Moreover, each port of the WESN's inputs and outputs is a complex scalar. The received i th OFDM symbol $\mathbf{y}_i(t) = [y_i^{(0)}(t), y_i^{(1)}(t), \dots, y_i^{(N_r-1)}(t)]^T$ is first fed into buffers. At the j th antenna's buffer, it collects N_{bf} samples from $y_i^{(j)}(t)$ to form the vector $[y_i^{(j)}(t - N_{bf}), y_i^{(j)}(t - N_{bf} + 1), \dots, y_i^{(j)}(t)]^T$. Thereafter, the vector is mapped into reservoirs through the input-layers. Meanwhile, reservoirs update their inner states and generate the output vector $\mathbf{z}_i(t) = [z_i^{(0)}(t), z_i^{(1)}(t), \dots, z_i^{(N_r-1)}(t)]^T$, where $\mathbf{z}_i(t) \in \mathcal{C}^{N_r}$ and \mathcal{C} represents the modulation constellation. The output corresponding to one input OFDM symbol is concatenated as a matrix $\mathbf{Z}_i = [z_i(0), z_i(1), \dots, z_i(N_c - 1)] \in$

$\mathbb{C}^{N_r \times N_c}$. Finally, it conducts the Fourier transform on \mathbf{Z}_i and quantifies the resulting frequency signal into modulation symbols according to the constellation \mathcal{C} , i.e., $\mathcal{Q}_{\mathcal{C}}(\mathbf{Z}_i \mathbf{F})$, where \mathbf{F} represents the Fourier transform matrix.

D. Training of WESN

Now we consider the training of the output layer of the WESN receiver. For ease of discussion, we start from the SISO channel when the channel Doppler shift f_D is assumed as zero. As discussed in Sec. II-B, we assume the first OFDM symbol is the training set. For the training framework defined in (17), we select the objective function f as the Frobenius norm induced distance and \mathcal{D} as the WESN. According to the dynamics and outputs of the ESN discussed in Sec. II-C, the WESN's outputs are calculated by $\mathbf{W}\mathbf{S}$, where $\mathbf{S} \in \mathbb{C}^{(N_n) \times N_c}$ stands for the reservoir states, and $\mathbf{W} \in \mathbb{C}^{1 \times (1+N_n)}$ is the readout weights. With a slight generalization in our notations, here N_n stands for the number of neurons plus the length of buffers. Therefore, similarly as (15), the readout weights of the WESN are updated by solving

$$\min_{\mathbf{W}} \|\mathbf{W}\mathbf{S}\mathbf{F} - \bar{\mathbf{x}}_0^T\|_2 \quad (25)$$

where $\mathbf{F} \in \mathbb{C}^{N_c \times N_c}$ represents the Fourier transform matrix, and $\bar{\mathbf{x}}_0 \in \mathbb{C}^{N_c}$ is the pilot symbols in which the subscript stands for the first OFDM symbol. The solution can be further written as the following closed-form,

$$\mathbf{W} \stackrel{(a)}{=} \bar{\mathbf{x}}_0^T (\mathbf{S}\mathbf{F})^+ \stackrel{(b)}{=} (\bar{\mathbf{x}}_0^T \mathbf{F}^H) \mathbf{S}^+ \quad (26)$$

where (a) holds when we assume the number of training symbols is greater than the number of neurons plus inputs. Moreover, through (b), the weights learning can be interpreted as fitting the outputs of WESNs to the waveform of the target OFDM symbols, since $\bar{\mathbf{x}}_0^T \mathbf{F}^H$ stands for a time domain signal.

We consider the extension to the MIMO channel with a zero Doppler shift. Compared to the SISO, the MIMO receiver is required to learn a way to mitigate the inter-streams interference. To this end, we introduce the pattern of training pilots for WESN as depicted in Fig. 5a which plots the design when $N_t = N_r = 4$. This pattern occupies the same number of resource blocks as the comb structured MIMO-OFDM pilots in Fig. 2b. By using this pilot pattern, the outputs of the WESN can be expressed as the matrix $\mathbf{Z} = [\mathbf{Z}_0, \mathbf{Z}_1, \mathbf{Z}_2, \mathbf{Z}_3]$, where the subscripts represents

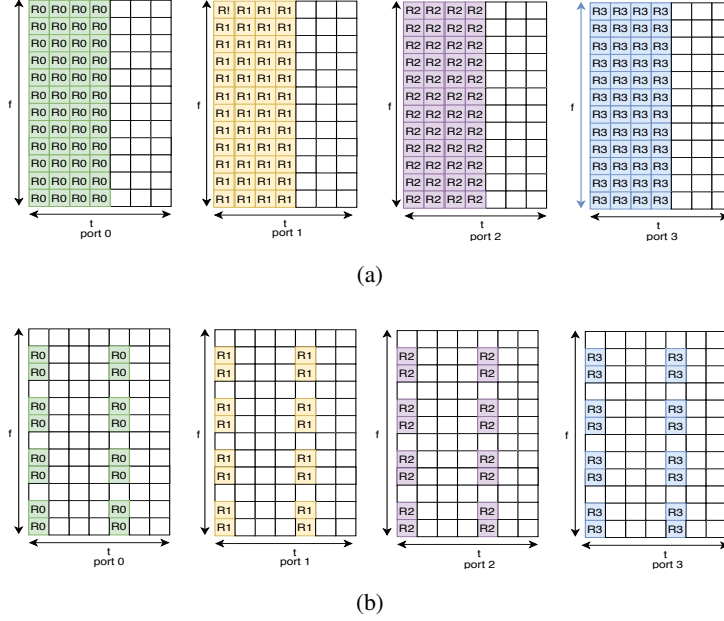


Fig. 5: OFDM Pilot Structure in one RB (a) Block (b) Scattered

the indices of the OFDM symbols allocated as pilots. Similarly, we know that $\mathbf{Z} = \mathbf{W}\mathbf{S}$, where $\mathbf{S} = [\mathbf{S}_0, \mathbf{S}_1, \mathbf{S}_2, \mathbf{S}_3] \in \mathbb{C}^{N_n \times 4N_c}$ represents the state matrix of the WESN. Similar to (25), the learning of the outputs layer is given by

$$\min_{\mathbf{W}} \|\mathbf{W}\mathbf{S}\mathbf{F}' - \bar{\mathbf{X}}\|_2 \quad (27)$$

where $\mathbf{F}' = \text{diag}(\mathbf{F}, \mathbf{F}, \mathbf{F}, \mathbf{F}) \in \mathbb{C}^{4N_c \times 4N_c}$ is a block diagonal matrix in which the diagonal element is \mathbf{F} ; $\bar{\mathbf{X}} = [\bar{\mathbf{X}}_0, \bar{\mathbf{X}}_1, \bar{\mathbf{X}}_2, \bar{\mathbf{X}}_3] \in \mathbb{C}^{N_r \times 4N_c}$ is the pilot symbols. Similarly, we have the solution

$$\begin{aligned} \mathbf{W} &= \bar{\mathbf{X}}[\mathbf{S}_0\mathbf{F}, \mathbf{S}_1\mathbf{F}, \mathbf{S}_2\mathbf{F}, \mathbf{S}_3\mathbf{F}]^+ \\ &\stackrel{(a)}{=} [\bar{\mathbf{X}}_0\mathbf{F}^H, \bar{\mathbf{X}}_1\mathbf{F}^H, \bar{\mathbf{X}}_2\mathbf{F}^H, \bar{\mathbf{X}}_3\mathbf{F}^H][\mathbf{S}_0, \mathbf{S}_1, \mathbf{S}_2, \mathbf{S}_3]^+ \end{aligned} \quad (28)$$

From (a), we know that the weight learning can be conducted in the time domain as well.

Now we consider the situation when the channel is with a Doppler shift. The pilots are designed to track the varying channel accordingly. To be compatible with the conventional pilots design in SISO depicted in the third sub-figure of Fig. 2a, we directly utilize this scattered pilots pattern as the training set of WESN. Therefore, the weights of the outputs are updated by

$$\min_{\mathbf{W}} \|\mathbf{W}[\mathbf{S}_0\mathbf{F}(:, \Omega_{f_0}), \mathbf{S}_4\mathbf{F}(:, \Omega_{f_4})] - [\bar{\mathbf{x}}_0^T(\Omega_{f_0}), \bar{\mathbf{x}}_4^T(\Omega_{f_4})]\|_2 \quad (29)$$

where Ω_{f_0} and Ω_{f_4} respectively represents the sub-carriers allocated to pilot symbols when $t = 0$ and $t = 4$ as shown in the figure. Alternatively, the above minimization problem can be expressed as

$$\min_{\mathbf{W}} \|\mathbf{W}[\mathbf{S}_0\mathbf{F}_{\Omega_{f_0}}, \mathbf{S}_4\mathbf{F}_{\Omega_{f_4}}] - [\bar{\mathbf{x}}_{0,\Omega_{f_0}}^T, \bar{\mathbf{x}}_{4,\Omega_{f_4}}^T]\|_2 \quad (30)$$

where

$$\bar{\mathbf{x}}_{t,\Omega_f}(n) \triangleq \begin{cases} \bar{\mathbf{x}}_t(n), & n \in \Omega_f \\ 0, & n \notin \Omega_f \end{cases} \quad (31)$$

$$\mathbf{F}_{\Omega_f}(n) \triangleq \begin{cases} \mathbf{F}(n), & n \in \Omega_f \\ \mathbf{0}, & n \notin \Omega_f \end{cases} \quad (32)$$

Therefore, the weights learning is given by

$$\mathbf{W} = [\bar{\mathbf{x}}_{0,\Omega_{f_0}}^T, \bar{\mathbf{x}}_{4,\Omega_{f_4}}^T][\mathbf{S}_0\mathbf{F}_{\Omega_{f_0}}, \mathbf{S}_4\mathbf{F}_{\Omega_{f_4}}]^+ \quad (33)$$

which can be rewritten as

$$\mathbf{W} = [\bar{\mathbf{x}}_{0,\Omega_{f_0}}^T \mathbf{F}^H, \bar{\mathbf{x}}_{4,\Omega_{f_4}}^T \mathbf{F}^H][\mathbf{S}_0\mathbf{F}_{\Omega_{f_0}} \mathbf{F}^H, \mathbf{S}_4\mathbf{F}_{\Omega_{f_4}} \mathbf{F}^H]^+ \quad (34)$$

where $\bar{\mathbf{x}}_{\Omega_f}^T \mathbf{F}^H$ represents the time domain OFDM waveform transformed merely from the symbols defined on the sub-carriers $\bar{\Omega}_f$. Therefore, the output weights are also learned by fitting the waveform of scattered pilots. Similarly, using the scattered pilots of MIMO illustrated in Fig. 5b, we have the following learning rule,

$$\mathbf{W} = [\bar{\mathbf{X}}_{0,\Omega_{f_0}}^T \mathbf{F}^H, \bar{\mathbf{X}}_{4,\Omega_{f_4}}^T \mathbf{F}^H][\mathbf{S}_0\mathbf{F}_{\Omega_{f_0}} \mathbf{F}^H, \mathbf{S}_4\mathbf{F}_{\Omega_{f_4}} \mathbf{F}^H]^+ \quad (35)$$

where $\bar{\mathbf{X}}_{t,\Omega_f}$ represents the MIMO pilots which is defined similarly as (31).

IV. COMPLEXITY ANALYSIS

In this section, we compare the computational complexity of the RC-based symbol detector to the conventional methods discussed in Sec. II-B. We divide the discussions into SISO and MIMO. Moreover, the time computational complexity is evaluated by floating-point operations per second (FLOPS).

A. SISO

1) *Channel Estimation:* For the conventional methods of solving the channel estimation problem (10), $g(\cdot)$ is assumed as a linear function. When $l(\cdot)$ is chosen as the mean squared error (MSE), we branch the channel estimation methods according to the pilot patterns plotted in Fig. 2 (a). For the comb pilots, the objective function in (10) is rewritten as

$$\min_{\tilde{\mathbf{h}}} \mathbb{E} \|\tilde{\mathbf{y}}_i - \bar{\mathbf{x}}_i \odot \tilde{\mathbf{h}}\|_F^2 \quad (36)$$

where \odot denotes the Hadamard product. From [35], we know that the solution is given by

$$\tilde{\mathbf{h}} = \mathbf{R}_{hy} \mathbf{R}_{yy}^{-1} \mathbf{y}_i \quad (37)$$

where $\mathbf{R}_{hy} = \mathbf{F} \mathbf{R}_{hh} \mathbf{F}^H \bar{\mathbf{X}}_i^H$, $\mathbf{X}_i = \text{diag}(\mathbf{x}_i)$, $\mathbf{R}_{yy} = \mathbf{X}_i \mathbf{F} \mathbf{R}_{hh} \mathbf{F}^H \mathbf{X}_i^H + \sigma^2 \mathbf{I}$, and \mathbf{R}_{hh} is the channel covariance matrix. For the scattered pilots, the channel coefficients on the time-frequency grids allocated as pilots are calculated by

$$\min_{\mathbf{h}(\Omega_f)} \mathbb{E} \|\tilde{\mathbf{y}}_i[\Omega_f] - \bar{\mathbf{X}}_i(\Omega_f) \mathbf{h}[\Omega_f]\|_F^2 \quad (38)$$

which has the closed-form solution as follows,

$$\mathbf{h}[\Omega_f] = \mathbf{R}_{hY}(\Omega_f) \mathbf{R}_{yy}(\Omega_f)^{-1} \tilde{\mathbf{y}}_i[\Omega_f] \quad (39)$$

where $\mathbf{R}_{hY}(\Omega_f) = \mathbf{F}(\Omega_f, :) \mathbf{R}_{hh} \mathbf{F}(\Omega_f, :)^H \bar{\mathbf{X}}_i(\Omega_f)^H$ and $\mathbf{R}_{yy}(\Omega_f) = \mathbf{X}_i(\Omega_f) \mathbf{F}(\Omega_f, :) \mathbf{R}_{hh} \mathbf{F}(\Omega_f, :)^H \mathbf{X}_i(\Omega_f, :)^H + \sigma^2 \mathbf{I}$. Thereafter, the channels on the rest grids are inferred by interpolation as discussed in [36]. Specifically, when the channel tap is assumed to be uncorrelated i.e., $\mathbf{R}_{hh} = \mathbf{I}$, we have

$$\tilde{h}[n] = \bar{x}_i^*[n] * \tilde{y}_i[n] / (|\bar{x}_i[n]|^2 + \sigma^2) \quad (40)$$

where n stands for the index of sub-carriers.

2) *Symbol Detection:* For the symbol detection problem (11), when $l(\cdot)$ is selected as MSE, we have

$$\min_{\mathbf{x}_i} \mathbb{E} \|\tilde{\mathbf{y}}_i - \mathbf{x}_i \odot \hat{\mathbf{h}}_i\|_F^2 \quad (41)$$

When the transmission symbols are uncorrelated between sub-carriers, (41) becomes

$$\min_{x_i[n]} \sum_{n=0}^{N_c-1} \mathbb{E} |\tilde{y}_i[n] - x_i[n] \hat{h}_i[n]|^2$$

which has the solution as follows

$$\hat{x}_i[n] = \hat{h}_i^*[n] * \tilde{y}_i[n] / (|\hat{h}_i[n]|^2 + \sigma^2) \quad (42)$$

3) *Complexity*: For complexity analysis, we first review the FLOPS of standard matrix operations. Given two matrices $\mathbf{A} \in \mathbb{C}^{m \times n}$ and $\mathbf{B} \in \mathbb{C}^{n \times p}$, the matrix product \mathbf{AB} requires $N_{FLOPS}(\mathbf{AB}) = 2mnp$ for the summations and additions. For any invertible matrix $\mathbf{C} \in \mathbb{C}^{n \times n}$, FLOPS of the inverse is $N_{FLOPS}(\mathbf{C}^{-1}) = n^3 + n^2 + n$. When $\mathbf{C} \in \mathbb{C}^{m \times n}$ is full column rank, FLOPS of the MP-inverse \mathbf{C}^+ is given by $3mn^2 + 2n^3$. Therefore, for the comb pilot pattern in Fig. 2b, the FLOPS of the LMMSE channel estimation (37) is $2N_c^2$, in which the calculation of the covariance matrices \mathbf{R}_{hy} and \mathbf{R}_{yy} are omitted. In the symbol detection stage (42), the FLOPS is proportional to N_c . Thus, the total FLOPS for the LMMSE channel estimation plus the symbol detection is on the scale of $\delta N_c^2 + (1 - \delta)N_c$, where δ represents the ratio of the pilot symbols to all the transmission symbols in the OFDM system. Moreover, when we consider the scattered pilot pattern in Fig. 2c, the complexity of interpolation needs to be included. For the standard linear interpolation method, the FLOPS is on the scale of $7N_c(1 - \kappa)$, where κ is the ratio of pilot sub-carriers over all sub-carriers. Thus, the total FLOPS for the LMMSE channel estimation with LMMSE symbol detection using scattered pilot is $\delta(\kappa N_c)^2 + \delta 7N_c(1 - \kappa) + (1 - \delta)N_c + \delta(1 - \kappa)N_c$.

For the ESN/WESN using comb pilots, according to (26), the FLOPS for the output weights learning is $2N_c(N_n + 1) + 3N_cN_n^2 + 2N_n^3$. Meanwhile, the calculation at the symbol detection stage is merely conducting the output layer mapping, where the FLOPS is N_nN_c . Thus, the overall FLOPS for the ESN/WESN based symbol detection is $\delta(2N_c(N_n + 1) + 3N_cN_n^2 + 2N_n^3) + (1 - \delta)N_nN_c$. For scattered pilots, FLOPS at the learning stage is $2(\kappa N_c)(N_n + 1) + 3\kappa N_cN_n^2 + 2N_n^3$. Therefore, the total number of FLOPS is proportional to $\delta(2(\kappa N_c)(N_n + 1) + 3\kappa N_cN_n^2 + 2N_n^3) + N_nN_c$. The resulting complexity of the ESN/WESN is linearly proportional to the number of subcarriers. It suggests that the ESN/WESN has less computational burden than the LMMSE method when the number of subcarriers is large. Remark that in this analysis, we do not consider the computations inside the reservoirs. This is because the reservoirs are usually implemented through analog circuits which perform faster than the digital circuit [37], [38] with less energy consumption.

B. MIMO

By using the comb and scattered pilots respectively plotted in Fig. 2b and Fig. 2c, the FLOPS of LMMSE channel estimation on each antenna pair is the same as the SISO case due to free interference. Therefore, the complexity of the MIMO channel estimation is N_tN_r .

times to the SISO case. However, for the symbol detection, the interference caused by multiple transmitted antennas are required to be annihilated. Thus, the MIMO symbol detection demands more computations than the SISO case.

Now, we consider the LMMSE MIMO symbol detection using (11). When the transmitted symbols on different sub-carriers are independent to each others, the symbol detection can be conducted in sub-carrier-wise. Therefore, at the n th sub-carrier of the t th OFDM symbol, the symbol detection is solved by

$$\min_{\tilde{\mathbf{x}}_i(n)} \mathbb{E} \|\tilde{\mathbf{y}}_i(n) - \hat{\mathbf{H}}_i(n)\tilde{\mathbf{x}}_i(n)\|_F^2 \quad (43)$$

which has the following closed-form solution

$$\tilde{\mathbf{x}}_i(n) = (\hat{\mathbf{H}}_i^H(n)\hat{\mathbf{H}}_i(n) + \sigma^2\mathbf{I})^{-1}\hat{\mathbf{H}}_i^H(n)\tilde{\mathbf{y}}_i(n) \quad (44)$$

Thus, the number of FLOPS is $2N_c(N^3 + N^2 + N)$, where N denotes the number of antennas at Tx and Rx when $N_t = N_r$.

For the MIMO sphere decoding, it is an approximation of solving the following maximum likelihood estimation,

$$\min_{\mathbf{x}_i(n) \in \mathcal{C}^{N_r}} \|\tilde{\mathbf{y}}_i(n) - \hat{\mathbf{H}}(n)\tilde{\mathbf{x}}(n)\|_2 \quad (45)$$

where \mathcal{C} represents the modulation constellation of the transmitted symbols. Since the standard sphere decoding usually has high redundancy in the implementation. We choose a complexity reduced sphere decoding algorithm proposed in [39] for the evaluation. It shows that the FLOPS is proportional to $N_c|\mathcal{C}|^N(2N^2 + 2N - 1)$ which implies the sphere decoding is extremely complicated when a high order modulation is adopted. Using the comb pilot for ESN/WESN, the FLOPS for output weight learning is $2N^2N_c(N_n + 1) + 3N_cNN_n^2 + 2N_n^3$ according to (28), where the number of training OFDM symbols is the same as the transmission antennas. At the symbol detection stage, FLOPS is N_cNN_n . Similarly, we can arrive at the FLOPS using the scattered pilot. The results of complexity comparison is summarized in Table I. We see that the computational complexity of ESN/WESN is dominated by the number of neurons which is smaller than N_c through the numerical experiments in Sec. V.

TABLE I: Computational Complexity of Symbol Detection Methods

Symbol Detection Method	Number of FLOPS
SISO LMMSE CSI with LMMSE	$\delta(\kappa N_c)^2 + \delta 7N_c(1 - \kappa) + (1 - \delta)N_c + \delta(1 - \kappa)N_c$
SISO ESN/WESN	$\delta(2(\kappa N_c)(N_n + 1) + 3\kappa N_c N_n^2 + 2N_n^3) + N_n N_c$
MIMO LMMSE CSI with LMMSE	$N^2(\delta(\kappa N_c)^2 + \delta 7N_c(1 - \kappa)) + (1 - \kappa\delta)N_c(N^3 + N^2 + N)$
MIMO LMMSE CSI with SD	$N^2(\delta(\kappa N_c)^2 + \delta 7N_c(1 - \kappa)) + (1 - \kappa\delta)N_c C ^N(2N^2 + 2N - 1)$
MIMO ESN/WESN	$\delta(2N^2\kappa N_c(N_n + 1) + 3\kappa N_c N N_n^2 + 2N_n^3) + N_c N N_n$

N : the number of antennas at Tx and Rx; δ : the ratio of pilot OFDM symbols; N_c the number of sub-carriers; κ is the ratio of pilot sub-carriers over all sub-carriers; N_n : the number of neurons and window.

V. PERFORMANCE EVALUATION

In this section, we evaluate the performance of WESN for the MIMO-OFDM symbol detection. Through our numerical experiments, we incorporate the model of RF circuits, such as up/downsamplers, PA, and anti-interference/alias filters into the link simulation. To simulate the analog domain, we apply four times up-sampling upon the baseband signal. Meanwhile, the number of paths, L , in the channel model (3) is set as 6. For any two different Tx-Rx antenna pairs in the the MIMO spatial channel, their paths coefficients are set to be independent. The base-band modulation order is selected as 16 QAM. For the conventional methods using scattered pilots, the CSI is obtained by a linear interpolation.

A. Overfitting Issue

Before proceeding on the comparison between the RC based receiver and the conventional methods, we first reveal the overfitting issue on selecting the number of neurons/reservoirs of the underlying RC based receiver. As shown in Fig. 6, we see that the BER of the training set decreases as the model becomes more complicated. At the same time, the BER gap between the testing set and the training set is enlarged as the number of neurons increases. Therefore, in order to achieve low generalization error (i.e., low BER on testing set), it requires a proper selection on the number of neurons.

B. SISO

We now consider the WESN in the SISO channel under different operation regions of PA. Fig. 7 shows the BER results when the Doppler shift is 0Hz, where the threshold for PA linear

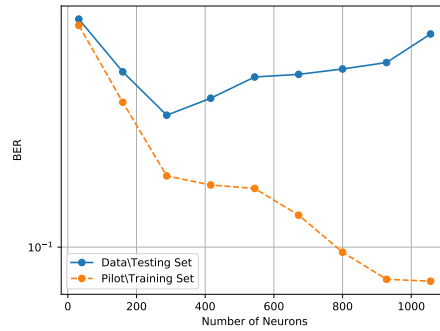


Fig. 6: The over-fitting issue of changing the number of neurons/reservoirs in ESN under block fading MIMO channel

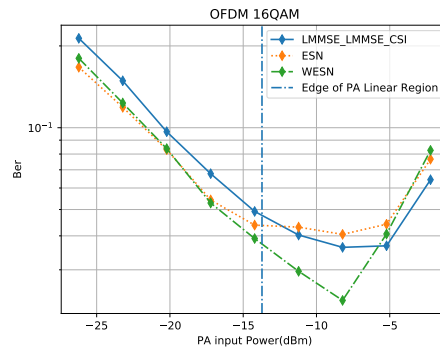


Fig. 7: BER comparison of ESN and WESN detectors with the conventional LMMSE method for SISO block fading channel

region is set as 3dB up to the boundary of the linear region as depicted in Fig. 1. Here the ESN is referred to as the buffer length of WESN is set as 1. The number of neurons for ESN and WESN is chosen to be the same, 64. The buffer length of WESN is set as 30. For, the labeled “LMMSE-LMMSE-CSI” method, the symbol detection is conducted by the LMMSE using the CSI obtained from the LMMSE channel estimation. We can observe that these three methods have comparable performance among the linear region. Moreover, for WESN, the BER performance is the best in PA nonlinear region when the optimal PA input power is selected. It demonstrates that the WESN can considerably compensate for the non-linear waveform distortion. We can also conclude that the symbol detection using the estimated CSI does not necessarily lead to the optimality in BER performance.

Nevertheless, the performance of the WESN is highly related to the settings of neural network parameters, especially the number of internal reservoirs and the buffer length. We further

investigate how the length of buffer and the number of neurons can jointly impact the BER performance. In Fig. 8. we observe that the length of buffer brings another degree of freedom to improve the symbol detection performance. From this figure, it shows that by either increasing the number of neurons or length of buffer, the resulting BER declines. However, due to the overfitting, BER increases again when the number of neurons becomes greater. Furthermore, it shows that compared to the WESN configured with more neurons, the WESN with few neurons and longer buffers can achieve the same performance. This is because the memory capacity of WESN is jointly determined by the configuration of the reservoir and the buffer.

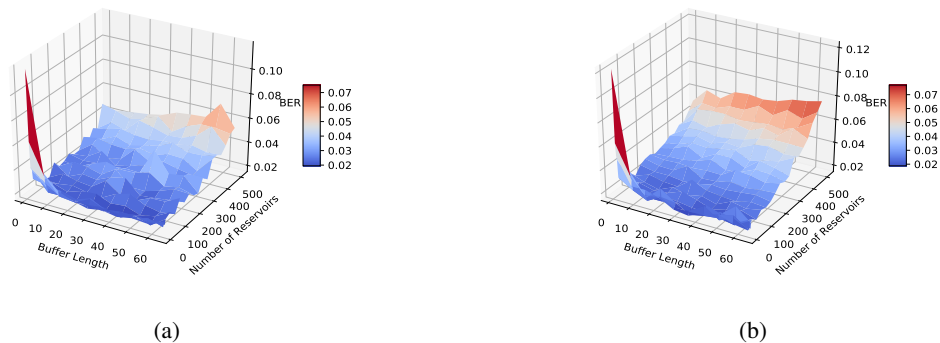


Fig. 8: The Average BER performance of SISO block fading channel by varying the length of buffer and the number of neurons: (a) 3D surface when PA input power is -8 dBm, (b) 3D surface when PA input power is -11 dBm, where the number of neurons varies from 8 to 512 and the buffer length ranges from 1 to 64.

Moreover, the BER performance under different Doppler shifts in the SISO channel is shown in Fig. 9. We see that these three methods are comparable in the BER as well. In Fig. 10, the comparison between ESN and WESN under different Doppler shifts is investigated. We can observe that the WESN always perform better than the ESN under different Doppler shifts. From Fig. 11, we again investigated the BER distribution by varying buffer length and neurons number. We see that increasing buffer size can significantly decrease BER which indicates that WESN can gain more advantages over the Doppler shift channel compared to the standard ESN. Meanwhile, adding more neurons can always lead to model overfitting.

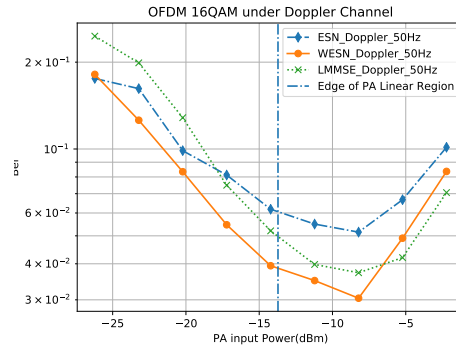


Fig. 9: BER comparison of ESN and WESN detectors with the conventional LMMSE method under SISO Doppler channel, where the number of neurons is set as 64, the buffer length is 30

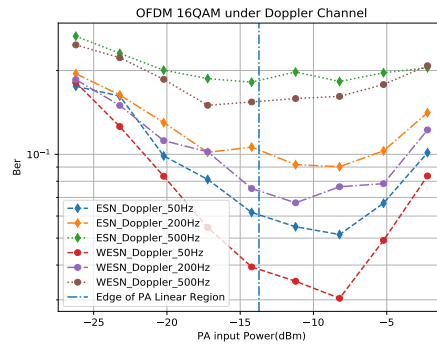


Fig. 10: BER comparison between ESN and WESN detectors under SISO Doppler channel with different Doppler shifts, where the number of neurons is set to be 64, the buffer length is 30

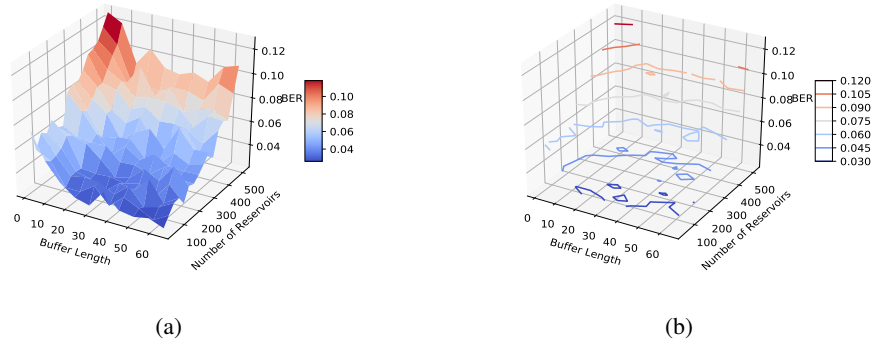


Fig. 11: The Average BER performance of WESN under SISO Doppler channel by varying buffer length and neurons number when the PA input power is -8 dBm, and Doppler shift is 50Hz: (a) 3D surface (b) 3D contour version

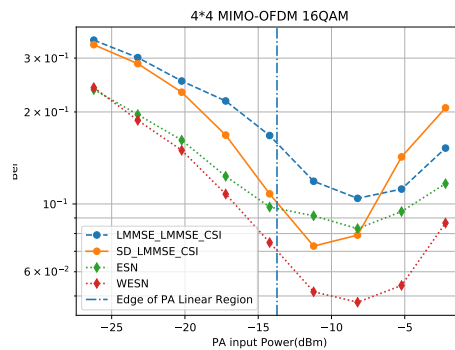


Fig. 12: BER comparison of ESN and WESN detectors with the conventional LMMSE and sphere decoding method for MIMO block fading channel

C. MIMO

In Fig. 12, we compare the BER performance of WESN to the conventional methods, i.e., LMMSE and sphere decoding (SD) under block fading channel. For the conventional methods, the CSI is obtained by LMMSE using the pilot patterns depicted in Fig. 2c. We see that the performance gap between WESN and SD and the conventional methods is enlarged compared to the SISO case. Especially, for SD, the BER performance deteriorates quickly when the PA input power is in the non-linear region. This is because SD requires more accurate CSI for symbol detection.

Again, we plot the BER distribution by varying the buffer length and the number of neurons as shown in Fig. 13. The advantages of the introduced buffer are more obvious compared to the SISO case by looking at Fig. 8. Moreover, by using the pilot pattern in Fig. 5a, the number of pilot symbols in training can be flexibly adjusted. In Fig. 14, we show the BER performance by varying the number of pilots, i.e., the number of OFDM symbols allocated as pilots. For instance, Fig. 5a shows the number of OFDM pilot symbols is equal to 4. Specifically, when $T < 4$, it is non-orthogonal pilots as the number of pilot OFDM symbols is smaller than the number of Tx antennas, 4. When we employ the conventional methods, using non-orthogonal pilot is not enough to avoid the pilot interference during the channel estimation stage. This means the conventional channel estimation method cannot be directly applied for non-orthogonal pilot. However, by using RC based method, we can observe that the BER performance is almost invariant compared to orthogonal pilots. It is because that the learning-based symbol detection can extract important features underlying the channel which are the inherent sparsity in the

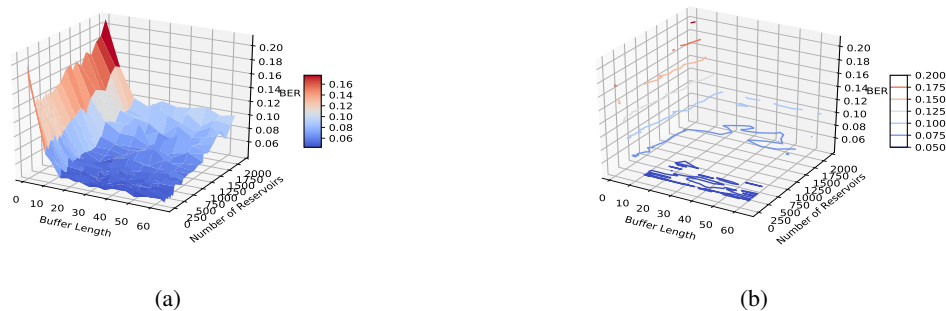


Fig. 13: The average BER performance in the MIMO block fading channel by varying buffer length and neurons number when the PA input power is -8 dBm: (a) 3D surface (b) 3D contour version

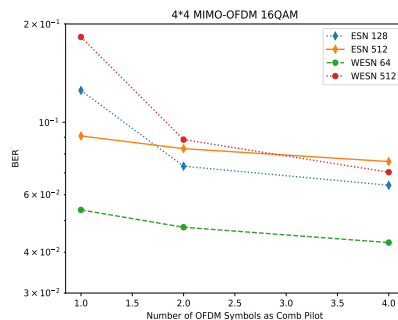


Fig. 14: The BER performance of ESN and WESN under MIMO block fading channel using comb pilot by varying the pilot length of OFDM symbols, where the PA input power is chosen as the -9dBm, the number of neurons for ESN is equal to 128 and 512, the number of neurons for WESN is equal to 64 and 512, the buffer length is 32.

time-delay domain. Meanwhile, by increasing the number of neurons, we can also observe the deterioration of BER performance due to the overfitting. In Fig. 15, we plotted the performance using the scattered pilot of MIMO under the Doppler shift channel. The 2D BER distribution under the Doppler channel is shown in Fig. 16 which has a similar distribution as Fig. 13.

VI. CONCLUSION

In this paper, we considered the application of reservoir computing, a special RNN, to MIMO-OFDM symbol detection. Compared to our previous work [29], a new RC based detector, WESN, is introduced as the receiver to significantly improve the performance of interference

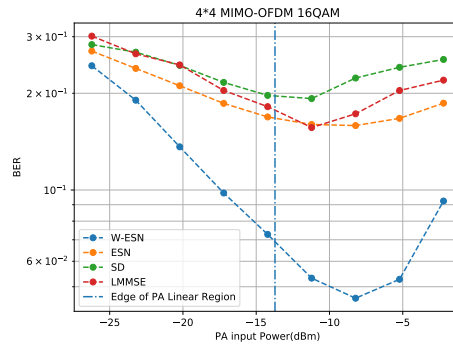


Fig. 15: BER comparison of ESN and WESN detectors with the conventional LMMSE and sphere decoding method for MIMO Doppler channel where the buffer length is 30, the number of neurons is 64 and the Doppler shift is 50Hz

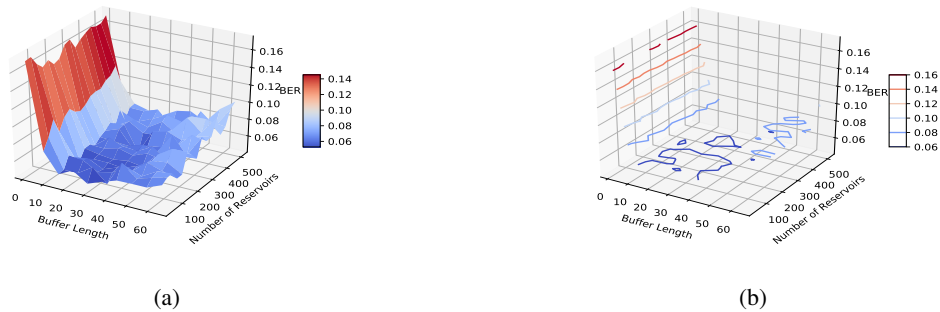


Fig. 16: The average BER performance under MIMO Doppler channel by varying the buffer length and neurons number, when the Doppler shift is 50Hz: (a) 3D surface, (b) 3D contour version

cancellation. As an extension to the standard ESN, which we utilized in our previous work, the added buffer of WESN proved to be able to fundamentally enhance the short term memory of the reservoir computing system. Additionally, compared to conventional coherent MIMO-OFDM symbol detection strategies as well as ESN, numerical evaluation demonstrates that WESN offers great performance improvement even under the constraint of using compatible pilot patterns defined in 3GPP LTE standards in both static and dynamic MIMO channel. Moreover, through complexity analysis, we prove that WESN performs relatively few FLOPS compared with conventional methods. Beyond the scope of this paper, we plan to extend our symbol detection framework to solve more comprehensive problems in communications systems, such

as the joint symbol demodulation and channel decoding.

APPENDIX

Proof of Theorem 4

From the previous discussion, we know the output weights for the i -delay capacity can be calculated by

$$\min_{\mathbf{w}_{output}} \|\tilde{\mathbf{y}}(m : N - 1) - \tilde{\mathbf{x}}(0 : N - m - 1)\|_2 \quad (46)$$

in which $\mathbf{y} = \mathbf{w}_{output} \mathbf{S}_{WESN}$, where $\mathbf{S}_{WESN} = [[\tilde{\mathbf{x}}^T(m : m - M), \mathbf{s}^T(m)]^T, [\tilde{\mathbf{x}}^T(m + 1 - M), \mathbf{s}^T(m + 1)], \dots, [\tilde{\mathbf{x}}^T(N - 1 - M), \mathbf{s}^T(N - 1)]]^T$. Therefore, we have

$$\|[\mathbf{w}_1, \mathbf{w}_2][\mathbf{X}^T, \mathbf{S}_{ESN}^T]^T - \tilde{\mathbf{x}}(0 : N - m - 1)\|_2 \quad (47)$$

$$= \|\mathbf{w}_1 \mathbf{X} - \lambda \tilde{\mathbf{x}}(0 : N - m - 1) + \mathbf{w}_2 \mathbf{S}_{ESN} - (1 - \lambda) \tilde{\mathbf{x}}(0 : N - m - 1)\|_2 \quad (48)$$

$$\leq \|\mathbf{w}_1 \mathbf{X} - \lambda \tilde{\mathbf{x}}(0 : N - m - 1)\|_2 + \|\mathbf{w}_2 \mathbf{S}_{ESN} - (1 - \lambda) \tilde{\mathbf{x}}(0 : N - m - 1)\|_2 \quad (49)$$

Thus

$$\min_{\mathbf{w}_1, \mathbf{w}_2} \|[\mathbf{w}_1, \mathbf{w}_2][\mathbf{X}^T, \mathbf{S}_{ESN}^T]^T - \tilde{\mathbf{x}}(0 : N - m - 1)\|_2 \quad (50)$$

$$\leq \min_{\mathbf{w}_1} \|\mathbf{w}_1 \mathbf{X} - \lambda \tilde{\mathbf{x}}(0 : N - m - 1)\|_2 + \min_{\mathbf{w}_2} \|\mathbf{w}_2 \mathbf{S}_{ESN} - (1 - \lambda) \tilde{\mathbf{x}}(0 : N - m - 1)\|_2 \quad (51)$$

$$= \lambda r_W + (1 - \lambda) r_{ESN} \quad (52)$$

where

$$r_W = \|\mathbf{w}_1 \mathbf{X} - \lambda \tilde{\mathbf{x}}(0 : N - i - 1)\|_2 \quad (53)$$

$$r_{ESN} = \|\mathbf{w}_2 \mathbf{S}_{ESN} - \tilde{\mathbf{x}}(0 : N - i - 1)\|_2 \quad (54)$$

Therefore, from the definition of STM, we have

$$MC_{WESN} \geq \lambda MC_W + (1 - \lambda) MC_{ESN}, \lambda \in (0, 1) \quad (55)$$

REFERENCES

- [1] L. Liu, R. Chen, S. Geirhofer, K. Sayana, Z. Shi, and Y. Zhou, "Downlink mimo in lte-advanced: Su-mimo vs. mu-mimo," *IEEE Commun. Mag.*, vol. 50, no. 2, pp. 140–147, February 2012.
- [2] S. Yang and L. Hanzo, "Fifty years of mimo detection: The road to large-scale mimos," *IEEE Commun. Surveys Tuts.*, vol. 17, no. 4, pp. 1941–1988, 2015.
- [3] Y. Rahmatallah and S. Mohan, "Peak-to-average power ratio reduction in ofdm systems: A survey and taxonomy," *IEEE Commun. Surveys Tuts.*, vol. 15, no. 4, pp. 1567–1592, 2013.
- [4] Dukhyun Kim and G. L. Stuber, "Clipping noise mitigation for ofdm by decision-aided reconstruction," *IEEE Communications Letters*, vol. 3, no. 1, pp. 4–6, Jan 1999.
- [5] H. Chen and A. M. Haimovich, "Iterative estimation and cancellation of clipping noise for ofdm signals," *IEEE Communications Letters*, vol. 7, no. 7, pp. 305–307, 2003.
- [6] D. R. Morgan, Z. Ma, J. Kim, M. G. Zierdt, and J. Pastalan, "A generalized memory polynomial model for digital predistortion of rf power amplifiers," *IEEE Trans. Signal Process.*, vol. 54, no. 10, pp. 3852–3860, 2006.
- [7] B. E. Watkins and R. North, "Predistortion of nonlinear amplifiers using neural networks," in *Proceedings of MILCOM'96 IEEE Military Communications Conference*, vol. 1. IEEE, 1996, pp. 316–320.
- [8] M. Rawat, K. Rawat, and F. M. Ghannouchi, "Adaptive digital predistortion of wireless power amplifiers/transmitters using dynamic real-valued focused time-delay line neural networks," *IEEE Transactions on Microwave Theory and Techniques*, vol. 58, no. 1, pp. 95–104, 2009.
- [9] J. Joung, C. K. Ho, K. Adachi, and S. Sun, "A survey on power-amplifier-centric techniques for spectrum- and energy-efficient wireless communications," *IEEE Commun. Surveys Tuts.*, vol. 17, no. 1, pp. 315–333, First Quarter 2015.
- [10] T. J. O'Shea, T. Erpek, and T. C. Clancy, "Deep learning based mimo communications," *arXiv preprint arXiv:1707.07980*, 2017.
- [11] T. O'Shea and J. Hoydis, "An introduction to deep learning for the physical layer," *IEEE Trans. on Cogn. Commun. Netw.*, vol. 3, no. 4, pp. 563–575, 2017.
- [12] S. Dörner, S. Cammerer, J. Hoydis, and S. t. Brink, "Deep learning based communication over the air," *IEEE J. Sel. Topics Signal Process.*, vol. 12, no. 1, pp. 132–143, Feb 2018.
- [13] N. Farsad and A. Goldsmith, "Neural network detectors for molecular communication systems," in *IEEE 19th Intl Workshop on Signal Processing Advances in Wireless Commun. (SPAWC)*. IEEE, 2018, pp. 1–5.
- [14] —, "Systems and methods for transmitting and receiving data using machine learning classification," Aug. 16 2018, uS Patent App. 15/896,982.
- [15] —, "Sliding bidirectional recurrent neural networks for sequence detection in communication systems," *arXiv preprint arXiv:1802.08154*, 2018.
- [16] B. Karanov, M. Chagnon, F. Thouin, T. A. Eriksson, H. Bülow, D. Lavery, P. Bayvel, and L. Schmalen, "End-to-end deep learning of optical fiber communications," *Journal of Lightwave Technology*, vol. 36, no. 20, pp. 4843–4855, 2018.
- [17] F. N. Khan, C. Lu, and A. P. T. Lau, "Machine learning methods for optical communication systems," in *Signal Processing in Photonic Communications*. Optical Society of America, 2017, pp. SpW2F–3.
- [18] H. Ye, G. Y. Li, and B. Juang, "Power of deep learning for channel estimation and signal detection in ofdm systems," *IEEE Commun. Lett.*, vol. 7, no. 1, pp. 114–117, Feb 2018.
- [19] J. Zhang, C.-K. Wen, S. Jin, and G. Y. Li, "Artificial intelligence-aided receiver for a cp-free ofdm system: Design, simulation, and experimental test," *arXiv preprint arXiv:1903.04766*, 2019.

- [20] P. Jiang, T. Wang, B. Han, X. Gao, J. Zhang, C.-K. Wen, S. Jin, and G. Y. Li, "Artificial intelligence-aided ofdm receiver: Design and experimental results," *arXiv preprint arXiv:1812.06638*, 2018.
- [21] X. Tan, W. Xu, Y. Be'ery, Z. Zhang, X. You, and C. Zhang, "Improving massive mimo belief propagation detector with deep neural network," *arXiv preprint arXiv:1804.01002*, 2018.
- [22] A. W. Neev Samuel, Tzvi Diskin, "Learning to detect," *arXiv preprint arXiv:1805.07631*, 2018.
- [23] C. Szegedy, W. Liu, Y. Jia, P. Sermanet, S. Reed, D. Anguelov, D. Erhan, V. Vanhoucke, and A. Rabinovich, "Going deeper with convolutions," in *Proceedings of the IEEE conference on computer vision and pattern recognition*, 2015, pp. 1–9.
- [24] I. Goodfellow, Y. Bengio, and A. Courville, *Deep learning*. MIT press, 2016.
- [25] P. J. Werbos *et al.*, "Backpropagation through time: what it does and how to do it," *Proceedings of the IEEE*, vol. 78, no. 10, pp. 1550–1560, 1990.
- [26] R. Pascanu, T. Mikolov, and Y. Bengio, "On the difficulty of training recurrent neural networks," in *International conference on machine learning*, 2013, pp. 1310–1318.
- [27] S. Hochreiter and J. Schmidhuber, "Long short-term memory," *Neural computation*, vol. 9, no. 8, pp. 1735–1780, 1997.
- [28] H. Jaeger, "The echo state approach to analysing and training recurrent neural networks—with an erratum note," *Bonn, Germany: German National Research Center for Information Technology GMD Technical Report*, vol. 148, no. 34, p. 13, 2001.
- [29] S. Mosleh, L. Liu, C. Sahin, Y. R. Zheng, and Y. Yi, "Brain-inspired wireless communications: Where reservoir computing meets MIMO-OFDM," *IEEE Trans. Neural Netw. Learn. Syst.*, vol. 29, no. 10, pp. 4694–4708, Oct 2018.
- [30] S. Mosleht, C. Sahint, L. Liut, R. Zheng, and Y. Yit, "An energy efficient decoding scheme for nonlinear mimo-ofdm network using reservoir computing," in *International Joint Conference on Neural Networks (IJCNN)*. IEEE, 2016, pp. 1166–1173.
- [31] R. Shafin, L. Liu, J. Ashdown, J. Matyjas, M. Medley, B. Wysocki, and Y. Yi, "Realizing green symbol detection via reservoir computing: An energy-efficiency perspective," in *IEEE International Conference on Communications (ICC)*, May 2018.
- [32] L. G. Barbero and J. S. Thompson, "Fixing the complexity of the sphere decoder for MIMO detection," *IEEE Trans. Wireless Commun.*, vol. 7, no. 6, 2008.
- [33] J. Joung, C. K. Ho, K. Adachi, and S. Sun, "A survey on power-amplifier-centric techniques for spectrum-and energy-efficient wireless communications," *IEEE Communications Surveys & Tutorials*, vol. 17, no. 1, pp. 315–333, 2015.
- [34] H. Jaeger, *Short term memory in echo state networks*. GMD-Forschungszentrum Informationstechnik, 2001, vol. 5.
- [35] S. Coleri, M. Ergen, A. Puri, and A. Bahai, "Channel estimation techniques based on pilot arrangement in ofdm systems," *IEEE Trans. Broadcast.*, vol. 48, no. 3, pp. 223–229, 2002.
- [36] X. Dong, W.-S. Lu, and A. C. Soong, "Linear interpolation in pilot symbol assisted channel estimation for ofdm," *IEEE Trans. Wireless Commun.*, vol. 6, no. 5, 2007.
- [37] F. Duport, A. Smerieri, A. Akrouit, M. Haelterman, and S. Massar, "Fully analogue photonic reservoir computer," *Scientific reports*, vol. 6, p. 22381, 2016.
- [38] K. Vandoorne, P. Mechet, T. Van Vaerenbergh, M. Fiers, G. Morthier, D. Verstraeten, B. Schrauwen, J. Dambre, and P. Bienstman, "Experimental demonstration of reservoir computing on a silicon photonics chip," *Nature communications*, vol. 5, p. 3541, 2014.

- [39] R. Y. Chang, W.-H. Chung, and S.-J. Lin, "A* algorithm inspired memory-efficient detection for mimo systems," *IEEE Wireless Commun. Lett.*, vol. 1, no. 5, pp. 508–511, 2012.